

# Towards the use of meshless methods to simulate brain growth in early development

---

Francesc Carandell Verdaguer



Universitat  
Pompeu Fabra  
*Barcelona*



# Towards the use of meshless methods to simulate brain growth in early development

Francesc Carandell Verdaguer

---

Bachelor's thesis UPF 2021/2022

Thesis supervisor(s):

Dr. Oscar Camara Rey

Mireia Alenyà Sistané

UPF tutor:

Dr. Oscar Camara Rey





## **Acknowledgments**

I would like to express my most sincere gratitude to my supervisors Oscar Camara and Mireia Alenyà for giving me the opportunity to undertake this project, and for their constant advice, guidance and dedication throughout all the year. I would also like to thank Carlos Albors for his knowledge and support during the development of the project. To all my friends for pushing me and being by my side whenever I needed them. And to my family for their unconditional support, tons of patience during all these years and the opportunity to study what I really love.

## **Abstract**

The process by which the brain develops from a smooth surface at early weeks of gestation to a folded surface with sulci and gyri at the neonatal stage is still an unsolved question. Despite the hypotheses proposed by several theories, the lack of large data at different developmental stages and limitations in computational resources have made it difficult to develop mechanical models of brain growth to better understand which mechanisms control the cortical folding process and test different hypothesis about the most relevant factors guiding this phenomenon. An additional challenge is to work with finite-element meshes (FEM) in this application, due to the large deformations undergone in brain development that can generate overlapping elements, which hamper obtaining the correct solutions and prevent the simulations to converge. Thus, meshless modelling techniques could give a solution to that issue since they are based on particles, not requiring node connectivity and being robust against complex mechanisms such as brain folding. The main goal of this TFG is setting the first steps that could allow modelling cortical folding through meshless methods. To do so, a Smoothed Particle Hydrodynamics (SPH) environment built for modelling cardiac mechanical motion was adapted in order to incorporate the mechanical equations that describe the gyrification process. Then, the results were assessed by making a comparison with the current FEM-based implementations in simplified synthetic scenarios.

## **Key words**

Brain development, Mechanical model, Gyrification, Meshless.

# Preface

Brain develops from a smooth surface into a highly folded structure during the foetal stage. This process, also known as gyrification, is considered complex and not well understood. Alterations during it can lead to severe neurodevelopment growth abnormalities. While 10% of children are affected by neurodevelopment alterations, one third of all disorders will be diagnosed after birth, which limits the time for their intervention. Therefore, there is a need for further understanding the brain cortical folding process.

Different hypotheses have been postulated so as to explain which are the mechanisms that drive gyrification. These theories have proposed that the skull constraints the brain's growth and generates a compressive force that folds the brain's surface, that two axons wired together can pull connected brain surface regions together or that complex genetic pathways generate a differential tissue growth that end up in the formation of folds. However, although any of these hypotheses exclude the others, the one that is considered as more likely is a differential growth between the cortex and subcortical layers. If the cortex is assumed to grow faster than the subcortical layers, a compressive force is generated and thereby folds are formed.

Gyrification has been studied in experimental setups to measure various physical parameters and, in some cases, they are coupled with computational modelling. These numerical approaches are becoming a powerful predictive tool that can propose new insights to better comprehend the brain's folding process. Mesh-based methods are the most used ones for their maturity and robustness. Nevertheless, they are not optimal for modelling high deformations, which are a feature encountered in gyrification and prevent obtaining the correct simulation. Thus, mesh-free techniques, overcoming these limitations by using unconnected particles representing the geometry, have the potential to be used for studying the brain's cortical folding process. However, such techniques have never been used in this context.

In this project, a framework for the study of cortical folding in the context of brain development through meshless methods is presented. A pre-processing pipeline for generating synthetic meshless models together with the adaptation of a mesh-based gyrification biomechanical model so as to be used in a meshless environment have been developed.





# Contents

<b>1. Introduction .....</b>	<b>1</b>
1.1. Foetal brain development .....	1
1.2. State of the art in mechanical modelling .....	4
1.3. Proposal and objectives .....	5
<b>2. Methods.....</b>	<b>6</b>
2.1. Smoothed Particle Hydrodynamics .....	6
2.1.1. SPH formulation.....	6
2.1.2. Equations of motion and Total Lagrangian formulation .....	7
2.2. Brain's gyrification biomechanical model .....	9
2.2.1. Cortical growth kinetics .....	9
2.2.2. Constitutive equations.....	11
2.3. Integration of the physical model in an SPH environment.....	12
2.4. Brain modelling and synthetic simulation setup .....	13
2.4.1. Geometry pre-processing .....	13
2.4.2. Particle's normal direction definition .....	15
2.4.3. Simulation setup.....	16
<b>3. Results .....</b>	<b>17</b>
3.1. Sensitivity analyses.....	17
3.1.1. Time step.....	17
3.1.2. Kernel size.....	19
3.1.3. Geometry's number of points.....	21
3.1.4. Normal vector direction's interpolation .....	22
3.2. Comparison between SPH and FEM results .....	23
<b>4. Discussion .....</b>	<b>26</b>
4.1. Geometries' pre-processing.....	26
4.2. Mechanical model inclusion in a SPH environment.....	27
4.3. Sensitivity analyses .....	27
4.4. SPH as a method for modelling brain's gyrification .....	28
4.5. Limitations .....	30
<b>5. Conclusions .....</b>	<b>30</b>
<b>Bibliography .....</b>	<b>32</b>

## List of figures

<b>Figure 1:</b> Representation of the stages of cortical folding. Image from [6].....	<b>1</b>
<b>Figure 2:</b> Hypotheses for the mechanical folding of the brain's cortex. Image from [6].....	<b>3</b>
<b>Figure 3:</b> Kernel function representation in a 2D spatial domain. Image from [34].....	<b>7</b>
<b>Figure 4:</b> Model geometry adaption from a mesh (A) to a meshless geometry of 32k points (B) and a reduced meshless geometry of 15k points (C).....	<b>14</b>
<b>Figure 5:</b> Graphic representation of the normal vector interpolation for a point P. Since $D1 < D2$ , particle P will take as normal direction the vector of line N1.....	<b>15</b>
<b>Figure 6:</b> Changes in the simulation's total duration when modifying the time-step size.....	<b>16</b>
<b>Figure 7:</b> Resulting deformed sphere for each simulation found in simulation time 0.0429 for A, B and C; and simulation time 0.0275 for D. A) Time-step = $0.5 \cdot 10^{-5}$ B) Time-step = $1 \cdot 10^{-5}$ C) Time-step = $2 \cdot 10^{-5}$ D) Time-step = $4 \cdot 10^{-5}$ . The usage of different axis in each case allows observing that in A there is no deformation, the points of high deformation in B and C (in warmer colours) are found at the same regions, and the escaping particles present the highest J in D.....	<b>19</b>
<b>Figure 8:</b> A) Changes of simulation's total duration when modifying the kernel size. B) Changes of iteration's duration for variations of kernel size.....	<b>20</b>
<b>Figure 9:</b> Resulting deformed sphere in each test found in simulation time 0.0390. The higher values of J (in red) are found on the cortical bulges. A) Kernel size = 3 mm B) Kernel size = 3.5 mm C) Kernel size = 4 mm D) Kernel size = 4.5 mm E) Kernel size = 4.75 mm.....	<b>20</b>
<b>Figure 10:</b> Changes of iteration duration when modifying the geometry number of particles..	<b>21</b>
<b>Figure 11:</b> Resulting deformed sphere in each test found in simulation time 0.0240 for A; and simulation time 0.0429 for B and C. A) Number of particles = 15000 B) Number of particles = 32000 C) Number of particles = 45000.....	<b>22</b>
<b>Figure 12:</b> Resulting deformed sphere in each test found in simulation time 0.0429. A) Number of divisions = 4 B) Number of divisions = 8 C) Number of divisions = 16 .....	<b>23</b>
<b>Figure 13:</b> Resulting deformed sphere in the last iteration from the SPH model after applying the 3D Delaunay triangulation (A,C), and FEM model (B,D). C and D show the geometry's interior by applying a normal cut with respect to the x axis .....	<b>25</b>
<b>Figure 14:</b> Values of J in the last iteration found in the SPH test after applying the 3D Delaunay triangulation (A,C) and FEM test (B,D). C and D show the geometry's interior by applying a normal cut with respect to the x axis. The highest values of J are presented in warm colours...	<b>25</b>

# List of tables

**Table 1:** Simulation’s differences when modifying the time step size. All simulation’s geometries presented a number of particles of 32000..... **17**

**Table 2:** Simulation’s differences when modifying the kernel size. All simulation’s geometries presented a number of particles of 32000..... **19**

**Table 3:** Differences observed when modifying the geometry’s number of points..... **21**

**Table 4:** Summary of the changes in computational time and convergence observed when changing the interpolation method..... **22**

**Table 5:** SPH simulation and geometry’s parameter configuration. In this table it is also displayed the computational time employed and the convergence in terms of the simulation time reached..... **23**

**Table 6:** Quantitative measures for comparing growth and cortical folding between SPH and FEM simulations..... **24**

# 1. INTRODUCTION

## 1.1. Foetal brain development

Brain development in foetal stage, which lasts during three trimesters, involve, in broader terms, the formation of a complete network composed of millions of neurons and connections from a slim cell layer [1]. As such, this process is generally regarded as complex, and structural abnormalities can appear in some cases during development. Neurodevelopment growth alterations will have an impact on the affected children's quality of life, showing impairments on basic physical, psychological, sensory, cognitive, speech and language skills [2]. Nowadays, 10% of children are affected by neurodevelopmental abnormalities [3]. Still, one third of all neurological disorders will only be detected during childhood [4], limiting the time window for possible interventions. Thus, only two thirds of them are diagnosed before birth. Therefore, there is a need for developing tools that allow a better understanding of how the normal foetal brain develops and why abnormal neurodevelopment appears in some cases.

During the second and third trimesters of pregnancy (weeks 16-40), the prenatal human brain undergoes a folding process that leads the initial smooth brain's surface becoming a highly convoluted structure [5]. This allows to augment the brain's surface to volume ratio [6], which is often correlated with brain function and disorders in this folding process can cause severe neurological disorders. Gyrification allows the formation of gyri (folds) and sulci (valleys) patterns. It has been observed that this process also follows some ordered steps (*Figure 1*). Primary folds appear the earliest and correspond to the major ones, which have been found to be conserved among species and place important landmarks [7]. These primary folds are subsequently divided and form secondary folds, which are generally conserved among individuals of the same species. Finally, third order folds are formed, which are unique for each individual and happen almost randomly [8].

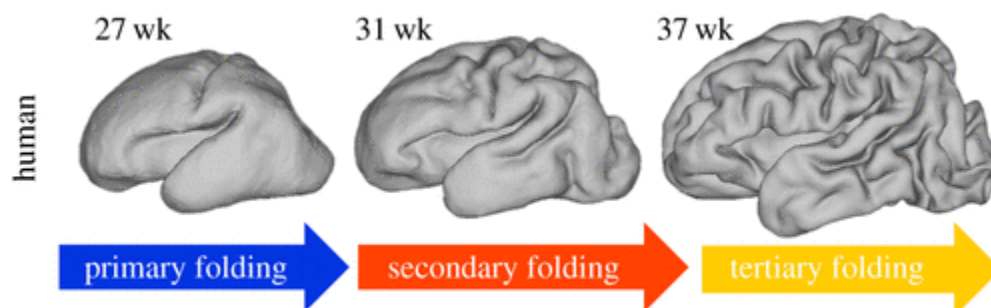


*Figure 1:* Representation of the stages of cortical folding. Image from [6].

Although gyrification needs the action of mechanical forces, the mechanisms that drive folding still remain uncertain. Different hypotheses have been postulated to explain which mechanisms control the cortical folding process [6] (*Figure 2*). On the one hand, it has been theorized that the skull applies a constraint for brain's expansion, which generates a compressive force on its surface that produces the brain's buckling and folding [9]. However, this idea has been generally disregarded as it has been shown that a skull's presence is not needed for the generation of folding patterns [10] and the skull's size will also be growing to allow the brain's development.

Axonal tension is generated when two axons wired together pull strongly connected cortical regions together [11]. Van Essen [12], following the observation that prenatal lesions affecting long-distance cerebral connections caused alterations in the folding patterns [13], proposed a model in which it was hypothesised that the tension between near-located cortical areas could generate a tangential force that induced the buckling of specific surface areas. The presence of said tensile stress has been experimentally demonstrated by different studies [11][14], and tested as a cortical folding driving force. Nevertheless, in the mentioned studies it was also concluded that axonal tension is not directed across developing gyri. However, this hypothesis needs further development, as the sole presence of tension between axons might have an impact in other processes, such as in the modulation of folds' shape [15][11].

The general brain development process, as in any other organ of the body, is orchestrated by complex genetic pathways that direct diverse processes such as cell proliferation, differentiation or migration [16]. During cortical folding, these patterns of gene expression might participate in the brain's surface buckling [17]. Therefore, it is believed that a phenotype associated to a specific gene expression might generate a differential tissue growth during tissue proliferation between surface areas, which finally conclude in the formation of cortical folds [18]. This genetic patterning is also contemplated as the reason why the primary and secondary folding processes are mostly conserved, since the cortical locations at which they appear are preserved [19]. In order to study the differences in the genetic expression between these proliferation patterns, microarray techniques were used so as to compare the transcriptome of cell progenitors in potential gyri in front of potential sulci in ferrets [20]. This analysis allowed the authors to identify thousands of differentially expressed genes between these two regions, further supporting the role of genetic patterning during gyrification.

Another hypothesized driver for gyrification, and also contemplated as the most likely one, is a differential growth between the cortical and subcortical layers [21]. The tangential expansion of the cortical layer with respect to the subcortical ones, which is produced since the grey matter is assumed to grow faster than the white matter layer, generates a compressive force that could induce mechanical instabilities that result in the buckling of the cortex [22]. It also has been shown that gyrification is determined by several physical parameters such as the primary geometry [23], the initial cortical thickness [24] or the relative growth between layers [25]. One property in which several authors have come to different conclusions, and might indicate the complexity of assessing the *in vivo* physical aspects of cortical folding, is the stiffness of both cortical and subcortical layers. On the one hand, some studies have suggested that white matter, found in the subcortical layer, is actually softer than gray matter initially, but stiffens over time [26], which indicates that there is a change of tissues' physical properties during gyrification. On the contrary, Xu *et al.* [11] found that the mechanical properties in both cortical and subcortical regions were very similar during the folding process in ferrets. Therefore, a much deeper understanding of the value and impact of these parameters is key in order to comprehend gyrification. However, the consequential folding pattern produced by models studying cortical folding using the differential tangential growth hypothesis are realistic in terms of size and shape [23], but it still has not been proved using real foetal brain geometries.

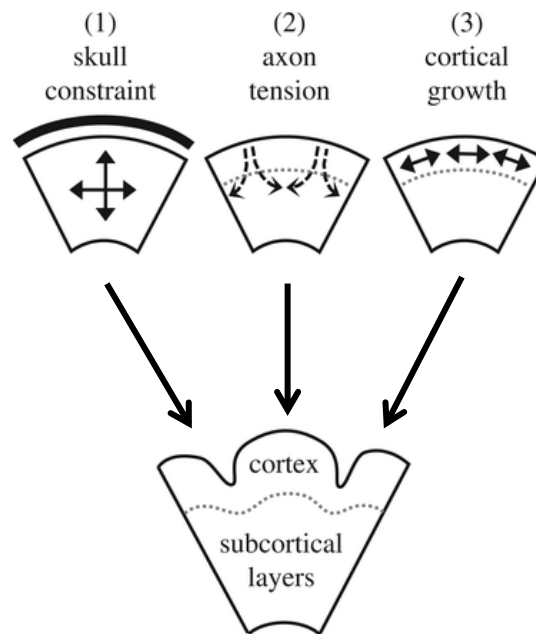


Figure 2: Hypotheses for the mechanical folding of the brain's cortex. Image from [6].

## 1.2. State of the art in mechanical modelling

The current research of the mechanics behind cortical folding has the aim of understanding the formation of gyri and sulci considering the physical properties and geometry shaping of the growing brain [27]. The latest advances in genomics have allowed shedding a light on the genetic pathways that regulate patterns of cortical growth [19][20]. However, the physics behind cortical folding remain unclear and only by performing experimental studies of neural mechanobiology coupled with computational modelling will allow assessing the different hypothesis postulated [6], as obtaining useful *in vivo* data from human foetal brains that enables the evaluation of said theories is still challenging [28].

The quantitative studies that use experimental setups to measure various parameters related to gyrification have permitted complementing the current theoretical and numerical paradigm. In the literature several works can be found that use experimental modelling to study, for instance, the effect of thickness and stiffness on cortical folding using polymer swelling experiments [21], the presence of folding with wavelength that depended on the thickness and modulus of the cortical layer using circular slices of gel [29] or differential growth using approximated 3D polydimethylsiloxane geometries that initially resembled the smooth foetal human brain [27].

In addition to experimental analyses, numerical approaches have also been used to test the different contemplated hypotheses. In most cases, the computational modelling of cortical folding has been based on the finite element method (FEM) [27][28][30]. FEM models make use of a geometry discretized in finite elements, also known as mesh, in which a set of partial differential equations describing the phenomenon studied are approximately solved in each of the elements by the minimization of an error function [31]. Tallinen *et al.* [27] proposed a human cortical model in which brain growth is modelled as a tangential expansion of the cortical layer with respect to the subcortical one, as it is assumed that the former is growing faster, which results in a differential growth. This mechanical model is able to simulate a realistic brain folding process by assuming that the brain is a neo-Hookean hyperelastic material, so it has been further used and developed in various recent studies [32][33]. Furthermore, Alenyà *et al.* [28] presented a whole computational pipeline to generate patient-specific finite-element 3D meshes from foetal magnetic resonance imaging (MRI) data to be then used to simulate and validate brain development through the aforementioned gyrification model. This pipeline permitted quantifying that there are still differences between the mechanical model and the observations.

Nevertheless, the use of FEM techniques in these mechanical models also introduces some challenges that limit the quality of the resulting folded brain simulations. They are mainly found in the requirement of meshes with elements of good quality, which is critical for the simulations' convergence; and the presence of large deformations that generate overlapping elements which hamper obtaining the correct solutions [28]. These ultimately lead to the need of manually editing the meshes to ensure convergence or introducing contact penalty forces that avoid the elements' collapse. It is in this context that meshless techniques can be used so as to cope with the aforementioned limitations since, as its own name indicates, meshless methods do not require the use of meshes to find solutions in structure-only models [34].

Meshless methods have been considered as an approach for modelling human biomechanics for their potential in simulating explicitly fluid flow and handling large deformations of soft materials [35]. These techniques have been used for the simulation of lateral collateral ligament [36], prediction of bone tissue remodelling [37], motion of deformable erythrocytes in flowing blood plasma [38] or a multi-physics model of the heart [34]. Therefore, for the study of brain cortical folding, in which large deformations and contact between elements are present, meshless methods, such as smooth particle hydrodynamics (SPH), can be tools to be tested to obtain results without requiring a rigorous mesh refinement process. However, there is not any study in which mesh-free geometries and meshless algorithms have been used to understand brain development and gyrification. Thus, there is in here an opportunity of a new field to be developed and explored.

### **1.3. Proposal and objectives**

The main goal of this project is generating a framework for the study of cortical folding in the context of brain development through meshless methods. To do so, several objectives can be described:

- I. Building of patient-specific brain meshless geometries.
- II. Adapting the current FEM biomechanical models so as to be used in a SPH environment.
- III. Evaluating the resulting folded geometry obtained from meshless simulations comparing it simulated FEM models in order to assess the overall performance of meshless methods for reproducing realistically the brain's folding process.



## 2. METHODS

In this part, first the developed meshless-based modelling pipeline will be described. Then, the next section describes in depth the brain's biomechanical model for cortical folding which has been adapted for meshless simulations in this work. The following part focuses on how the aforementioned physical model has been integrated inside the meshless software tool used. The last section presents how the geometry models have been obtained and the setup needed to carry out the meshless simulations.

### 2.1. Smoothed Particle Hydrodynamics

As it was commented before, the reduced accuracy when modelling large deformations of soft materials in mesh-based numerical methods limited the obtained results in previous gyrification's modelling studies. Using meshless methods, in the case of this work it was chosen Smoothed Particle Hydrodynamics (SPH) because of its versatility, maturity and large deformations' handling in comparison to other mesh-free methods [34]. According to the SPH formulation, the geometry is not discretized in a mesh but in a point cloud which contains particles with defined material physical properties but without any connectivity among them.

#### 2.1.1. SPH formulation

SPH is defined as a Lagrangian meshless method which discretizes the domain in a set of points with no connectivity [34]. The value of a smooth continuous function  $g$  in a particle of interest  $i$  can be calculated as:

$$g_i = \sum_j m_j \frac{g_j}{\rho_j} W_h(x_i - x_j), \quad (1)$$

where sub-index  $j$  indicates a particle in the neighbourhood of point  $i$ ,  $m$  and  $\rho$  are the particle's mass and density, respectively, and  $W_h(x_i - x_j)$  is the kernel function. The gradient with respect to space can be approximated as a derivative of the kernel function:

$$\nabla g_i = \sum_j m_j \frac{g_j - g_i}{\rho_j} \nabla W_h(x_i - x_j). \quad (2)$$

The kernel function is used to define which interactions are present between particle  $i$  and its neighbours (see *Figure 3*). This function depends on the smoothing length ( $h$ ), which defines the supported domain of definition of the kernel function. In other words,  $h$  will determine the number of neighbour particles that will be taken into account. Finally, the kernel function will be evaluated depending on the particles' positions ( $x$ ).

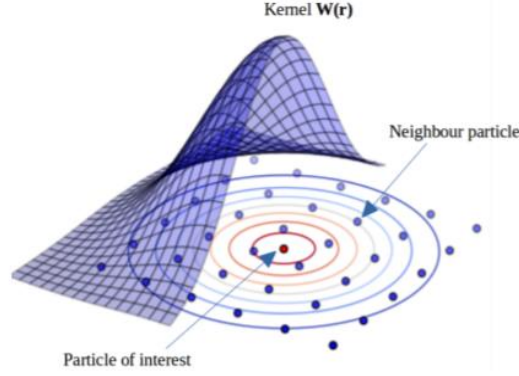


Figure 3: Kernel function representation in a 2D spatial domain. Image from [34].

### 2.1.2. Equations of motion and Total Lagrangian formulation

The motion of a body in isothermal conditions which is under the effect of external forces can be described using the momentum equation and the continuity equation:

$$\frac{d\rho}{dt} + \rho \frac{\partial v}{\partial x} = 0 \quad (3)$$

$$\rho \frac{dv}{dt} = \rho b + \frac{\partial \sigma}{\partial x}, \quad (4)$$

where  $t$  is time,  $\rho$  is the density,  $v$  the velocity vector,  $x$  the position vector,  $b$  the external forces and  $\sigma$  the stress tensor. As it has been explained, in the SPH formulation the geometry is discretized into particles of constant mass. Then, the density and velocity for each of the particles is updated by explicitly integrating *Equation 3* and *Equation 4*, while the displacement is updated after integrating in time the velocity's derivative.

By discretizing the continuity equation (*Equation 4*) using the SPH formulation (*Equation 1*), the density's material derivative of a particle of interest is obtained:

$$\frac{d\rho_i}{dt} = \sum_j m_j (v_i - v_j) \cdot \nabla_i W_{ij} . \quad (5)$$

On the other hand, the momentum equation's (*Equation 3*) discretization with SPH allows computing the acceleration of a particle of interest:

$$\frac{dv}{dt} = \sum_i m_i \left( \frac{p_i}{\rho_i^2} - \frac{p_j}{\rho_j^2} + \frac{S_j}{\rho_j^2} - \frac{S_i}{\rho_i^2} + \Pi_{ij} \right) \nabla_i W_{ij} + b, \quad (6)$$

where  $p$  stands for the hydrostatic pressure. The deviatoric stress tensor  $S$  also needs to be added for simulating solid mechanics. Finally,  $\Pi_{ij}$  represents the artificial viscosity, which is used in the SPH in order deal with numerical instabilities originated from local particle oscillations:

$$\Pi_{ij} = \begin{cases} \frac{-\alpha \bar{c}_{ij} \phi_{ij} + \beta \phi_{ij}^2}{\bar{\rho}_{ij}} & \phi_{ij} < 0 \\ 0 & \phi_{ij} \geq 0 \end{cases} \quad (7)$$

with

$$\phi_{ij} = \frac{\bar{h}_{ij}(v_{ij} \cdot r_{ij})}{|x_i - x_j|^2 + 0.01 \bar{h}_{ij}^2} ; \quad \bar{g}_{ij} = \frac{g_i + g_j}{2} \quad \text{for } g = c, \rho, h ,$$

where  $\alpha$  and  $\beta$  are the coefficients of artificial viscosity and are chosen to be 0.04 and 0.08 respectively, and  $c$  is the wave speed related to the material's stiffness.

Due to the interpolation technique used in SPH, a numerical artifact called tensile instability appears, which is especially perceptible when simulating solids in tension states [40]. To deal with it, a total Lagrangian formulation is used. Using this formulation, the reference configuration does not change throughout the simulation, and it is only used in order to calculate accelerations and stresses, which will update the position and velocity of the particles. Therefore, the motion of the body at any time  $t$  will be described by the mapping between the reference configuration and the present configuration:

$$\phi: \Omega_0 \rightarrow \Omega_t , \quad x = \phi(X, t).$$

Now, the motion in this configuration will follow the next conservation laws:

$$\rho_i = \frac{\rho_0}{J_i} \quad (8)$$

$$\frac{\partial^2 U_i}{\partial^2 t} = \frac{1}{\rho_0} \sum_j V_j (P_j - P_i - \Pi_{0ij}) \nabla_0 W_i (X_i - X_j) + b_i, \quad (9)$$

where  $U$  represents the displacement between configurations,  $P$  is the first Piola-Kirchhoff stress tensor and  $J$  is the determinant of the deformation gradient  $F$ :

$$J = \det(F), \quad F_i = \sum_j V_j (x_j - x_i) \nabla_0 W_i (X_i - X_j) \quad (10)$$

## 2.2. Brain's gyrification biomechanical model

The studied brain's cortical folding model was proposed by Tallinen *et al.* [27], which was able to realistically replicate the highly nonlinear mechanics behind brain folding phenomenon using the finite-element methodology. The model assumes that two different materials in contact that presented different growth rates, would induce mechanical instabilities that result in the buckling of the cortical layer. This model uses brain geometries discretized into a mesh composed of tetrahedral finite elements.

### 2.2.1. Cortical growth kinetics

The model enforces growth by expanding the elements sizes while maintaining their shape and topology. The differentiation between the cortical layer, which represents grey matter, and the subcortical one, the white matter, is made applying the following indicator function:

$$\theta(y) = \frac{1}{1 + e^{10(y/h-1)}}. \quad (11)$$

In *Equation 11*,  $y$  corresponds to the distance from surface using material coordinates; and  $h$  is the cortical thickness. Using this indicator function, the two materials are defined, with a smooth transition from the cortical layer ( $\theta = 1$ ) to the white matter zone ( $\theta = 0$ ).

The tangential cortical expansion ratio, which is the relative tangential growth ratio between the cortical and subcortical layers, is defined as:

$$g(y) = 1 + \alpha_t \theta(y)t, \quad (12)$$

where  $\alpha_t$  defines the cortical growth as  $\alpha_t = \sqrt{8} - 1$ , and  $t \in [0,1]$  parameterizes time. The corresponding growth tensor  $G$  is used to describe the tangential expansion perpendicular to each element's normal vector  $\hat{n}$ :

$$G = g(y)I + [1 - g(y)]\hat{n} \otimes \hat{n} . \quad (13)$$

On the other hand, it is also assumed that the cortical thickness ( $H$ ) will be increasing linearly as a function of time along the simulations time steps [28], which is a difference with respect to the original proposed model:

$$H = H_i + \beta t , \quad (14)$$

where  $H_i$  is the initial cortical thickness and  $\beta$  a constant factor empirically defined to be 0.3.. Furthermore, since there was a volume growth during cortical folding, it was needed to isotropically scale the reference state so that its longitudinal length changed accordingly:

$$L = 59 / (1 - 0.55t) \quad (mm). \quad (15)$$

However, Wang *et al.* [32] noticed that the Equation 15 was not completely realistic with the volume growth process found in biological measurement results. They modified it by introducing a second order term, which helped better scaling the longitudinal length with the biological observation:

$$L = -0.067(GA)^2 + 7.16(GA) - 66.05 \quad (mm), \quad (16)$$

where GA corresponds to the gestational age and it is related to the time of the model ( $t$ ) through the following equation:

$$t = 0.987e^{e^{-0.134(GA-29.433)}} \quad (17)$$

### 2.2.2. Constitutive equations

The brain is assumed to be a neo-Hookean hyperelastic material, which implies a non-linear relation between the stress and strain, described by the following strain energy density

$$W = \frac{\mu}{2} [Tr(FF^T)J^{-2/3} - 3] + \frac{K}{2} (J - 1)^2, \quad (18)$$

where  $\mu$  corresponds to the shear modulus,  $K$  is the bulk modulus,  $F$  is the corresponding deformation gradient and  $J = \det F$ . In the model, the bulk modulus is assumed to be  $K = 5\mu$ , which describes a modestly compressible material. It was also assumed that the cortical layer is slightly softer than the white matter area, presenting a shear modulus ratio between the two of  $\mu_c/\mu_w = 0.86$ . The shear modulus across the geometry can be calculated as:

$$\mu(y) = \theta(y)\mu_c + [1 - \theta(y)]\mu_w, \quad (19)$$

which show anisotropic properties for each of the elements depending on their relative position from surface.

The deformation gradient ( $F$ ) equation allows integrating the tangential growth tensor ( $G$ ) in the deformed configuration of a tetrahedral element ( $A$ ), which represents the stress-free initial configuration for the tetrahedron:

$$F = A(G\hat{A})^{-1}. \quad (20)$$

Finally, the Cauchy stress tensor, which defines the stress state at a point in the deformed state, is:

$$\sigma = \frac{1}{J} \frac{\partial W}{\partial F} F^T. \quad (21)$$

In order to deal with the element contacts at the brain surface, they were modelled using a penalty-based vertex-triangle contact processing [39]. In essence, this contact force avoids nodes from penetrating element faces and only occurs if the distance between a node and a superficial face is less than a given threshold and the calculated elastic force at a given time step would bring even closer.

### 2.3. Integration of the physical model in an SPH environment

The SPH environment used in this work was developed by Lluich *et al.* in [34], where a fully coupled multi-physics meshless model of the heart was constructed. The code allows coupling cardiac sub-models (electrophysiological, circulation and mechanical), which they are described by the SPH formulation presented previously. The only sub-model that needed to be adapted for this work was the 3D mechanical model. Thus, the mechanical solver had to be isolated from the other cardiac models, since we are only interested in modelling brain mechanical growth, and the complete physical model described in *Section 2.2.* had to be correctly introduced.

Regarding the solver detachment from the other models present in the SPH environment, it was found that several models acted as boundary conditions for the 3D mechanical model, modifying particles' parameters that had an impact on the computation of their acceleration and position during the simulation's iterations. What was done was basically eliminating these boundary conditions and re-computing the needed mechanical variables for each of the particles according to the brain mechanical model. For instance, in the cardiac 3D mechanical model the presence of a pericardium acted as a boundary condition that limited the movement of the external layer's particles. Therefore, this restriction was removed and substituted by a "free space", since in the studied brain mechanical model there is not a motion limitation of this kind. Another feature that was present in the original biomechanical model and was not incorporated into the adapted one is the contact processing penalty function among elements, since the SPH formulation uses unconnected particles and there was no need of maintaining a mesh topology.

In order to adapt the cortical growth kinetics described in *Section 2.2.1*, several approximations were made. First, the indicator function (*Equation 11*) was approximated so as to only define two materials: grey matter found in the external layer and white matter in the subcortical one. This approximation was introduced to diminish the computational time required to complete the simulations, since the distance to surface for each particle ( $y$ ) had to be obtained in each iteration. This implied first computing the distance of each inner particle to all the particles in the outer layer and then only taking the minimum value among these distances in every case. The value of the cortical thickness ( $H$ ) was also assumed to be constant and only used for initially assigning the layer to each of the particles. This decision was taken since this parameter only has an impact on the indicator function, which now is approximated to be binary and only used in the initial conditions ( $t=0$ ). With a similar reasoning, each particle's shear modulus ( $\mu$ ) and bulk modulus ( $K$ ) are not changed along the simulation's time since they now depend on the new indicator function. The tangential cortical expansion ratio ( $g(y)$ ) and growth tensor ( $G$ ) were computed and updated for each particle and iteration according to *Equation 12* and *Equation 13*, respectively.

Since the deformation gradient ( $F$ ) has to be now computed using the SPH formulation (*Equation 10*), the deformation gradient used in Tallinen's brain model (*Equation 20*) needed to be adapted, considering that in meshless methods there are not any tetrahedrons and, therefore, the stress-free initial configuration ( $A$ ) of each element could not be calculated. The deformation gradient was computed using the following equation, which allows integrating each particle's tangential growth tensor in the deformation gradient using the SPH formulation.

$$F_i = \left( \sum_j V_j (x_j - x_i) \nabla_0 W_i(X_i - X_j) \right) \cdot G . \quad (22)$$

Then, as the brain is assumed to be a neo-Hookean hyperelastic material, the strain energy density function used was the same as in *Equation 18*. This function was needed in order to first calculate the Cauchy Green stress tensor ( $\sigma$ ) and then it was used to compute the first Piola Kirchhoff stress tensor ( $P$ ), which was the one employed by the SPH environment for updating the particles' acceleration.

$$\sigma = \frac{1}{J} \frac{\partial W}{\partial F} F^T = \frac{\mu}{J^{\frac{5}{3}}} \left( F F^T - \frac{1}{3} \text{Tr}(F F^T) I \right) + K(J - 1) , \quad P = \sigma \cdot F^{-T} \cdot J . \quad (23)$$

## 2.4. Brain modelling and synthetic simulation setup

For the first simulations, the models were spheres of 12.496 mm radius as an approximation of a brain geometry, in a similar fashion as it has been done previously in other studies working in brain modelling [27][33].

### 2.4.1. Geometry pre-processing

To construct mesh-free geometries, the initial step is generating a mesh model with the desired shape. In this case, the synthetic sphere model was built by first generating a superficial mesh using Meshmixer<sup>1</sup> and then generating the respective volumetric mesh using Gmsh<sup>2</sup>. Then, the meshed model is transformed into a meshless geometry using Paraview<sup>3</sup>. Finally, in order to control the number of points in the model, a Python<sup>4</sup> algorithm is used. Essentially, this code randomly selects a specified number of particles to build the geometry and checks that the

---

<sup>1</sup> Meshmixer version 3.5

<sup>2</sup> Gmsh versión 4.9.5

<sup>3</sup> Paraview version 5.10.0

<sup>4</sup> Python version 3.3.2



density of points in all parts of the model is approximately uniform. A representation of the whole process can be found in *Figure 4*.

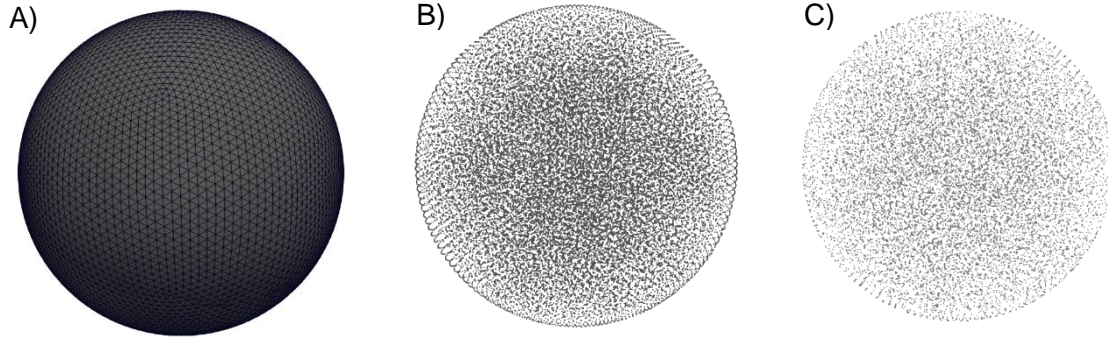


*Figure 4:* Model geometry adaption from a mesh (A) to a meshless geometry of 32k points (B) and a reduced meshless geometry of 15k points (C).

As it has been stated in *Section 2.2*, the brain's gyrification biomechanical model defines different material properties depending on the indicator function (*Equation 11*). Therefore, it is important to first determine the points found on the external layer. For the spheres, this is done by checking if each of the particles fulfills the following condition:

$$\frac{x^2}{r_x^2} + \frac{y^2}{r_y^2} + \frac{z^2}{r_z^2} \geq \lambda ,$$

( 24 )

where  $x, y$  and  $z$  represent the particle's coordinates,  $r_x, r_y$  and  $r_z$  are half the difference between the maximum and minimum value for each respective axis found on the particles' coordinates forming the cloud point; and  $\lambda$  represents the layer threshold. In a model where all particles were white matter, this threshold would be  $\lambda = 1$ . Nevertheless, as an external layer definition is needed, this margin has been defined as  $\lambda = 0.75$  in order to define said outer layer. Another approximation is done when defining the values for  $r_x, r_y$  and  $r_z$ . Their theoretical value would always correspond to the sphere's radius, but since the geometry is discretized in a finite number of unconnected points their values are adapted depending on the cloud of particles. Once the external layer is determined, those particles that do not fulfill the aforementioned condition will establish the internal layer.

The area of each of the particles is computed by dividing the total area of the geometry by the number of particles in the cloud of points. For obtaining the volume of each particle, the geometry's total volume can be expressed as:

$$V_{total} = \sum_{i=0}^{\# particles} V_i = k \cdot \sum_{i=0}^{\# particles} \frac{1}{N_i} , \quad (25)$$

where  $V_i$  and  $N_i$  are the volume and number of neighbours of particle  $i$ . The neighbours of particle  $i$  are those particles which are within a fixed distance from particle  $i$ . From the last equation,  $k$  can be isolated and computed for each model, as the total volume and the number of neighbours for each of the particles is known. Then, the volume of a single particle  $i$  is:

$$V_i = k \cdot \frac{1}{N_i} . \quad (26)$$

#### 2.4.2. Particle's normal direction definition

It is important to characterize the initial normal direction for each of the particles, as it is required to update their position and acceleration during the model's simulation. To do so, the normal vectors defined by the elements found on the sphere's mesh surface can be extracted using Paraview. Using an own designed Python code, the particles' normal vector can be interpolated by first dividing the geometry into a finite number of equal pieces containing the coordinates of the model's particles and the mesh's surface normal vectors enclosed in each of the portions. Then, the minimum distance of each particle to the line defined by each normal vector is computed. Finally, each particle's normal direction is approximated by taking the vector of the line with the least distance to the particle's coordinates. Therefore, all the initial normal directions will radially point towards the geometry's external surface.

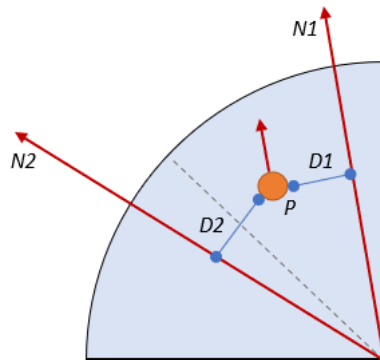


Figure 5: Graphic representation of the normal vector interpolation for a point  $P$ . Since  $D1 < D2$ , particle  $P$  will take as normal direction the vector of line  $N1$ .

### 2.4.3. Simulation setup

All simulations have been performed using Code::Blocks<sup>5</sup>, employing a computer laptop composed by 8 cores Intel Core i7-11800H and a Nvidia GeForce RTX 3050 Ti graphic card. In order to set both the simulation's parameters and the geometry characteristics, some have remained constant throughout the tests while others have been adjusted by performing a sensitivity analysis for each of them, which allowed assessing which was their impact on the simulations' resulting solution and choosing the best simulation setting (see *Section 3.1*).

Among the fixed parameters among all simulations, it can be remarked the kernel type, the time integration method and the geometry's cortical thickness. The kernel type defines the kernel function used in order to determine how each of the particles interacts with its neighbours in each iteration. The selected function has been the C<sup>2</sup>-Wendland Kernel because it has been observed that the results are more similar to the ones obtained in FEM simulations for mechanic simulations [34]. The time integration method applied is Runge Kutta 4, because it was observed to be appropriate in the context of SPH [41]. The geometries' external layer elongation is defined by the threshold  $\lambda$  from *Equation 22*. It was set to  $\lambda = 0.75$ , which corresponds to a cortical thickness of 10.82 mm. Since the number of layers in the model were approximated to only two, a more extended external layer was defined so as to better observe the resulting deformation.

On the other hand, the parameters studied in sensitivity analyses have been the time-step size, kernel size, geometry's number of particles and the number of symmetrical pieces in which the sphere was initially divided to interpolate the normal vector direction for each point. The study of the time-step size was needed because it determines the incremental change in time for which the equations are being solved and it has an influence on the solution's convergence and the simulation's duration. The kernel size is used to establish the maximum distance that the kernel function has an influence on, thereby determines the number of particles that will act as neighbours for each point. The geometry's number of particles defines the spatial resolution of the geometry's discretization, which has an impact on the solution's accuracy and the computational time employed. Last but not least, it was also studied if the number of fragments that the sphere was divided in for interpolating the initial normal vectors have an impact on the resultant solution and if this approximation adds a significant error on the results.

---

<sup>5</sup> Code::Blocks IDE version 20.3

### 3. RESULTS

The results are presented in two parts: four sensitivity analyses to better understand the impact of different parameters into the simulation's outcome and choosing the best combination of them; and a qualitative and quantitative comparisons between the SPH simulations and FEM simulations using Tallinen's model [27] to assess if the gyrification equations were correctly introduced, and evaluating the differences between these two modelling methodologies.

#### 3.1. Sensitivity analyses

The sensitivity analyses have been done in terms of running time and convergence. To evaluate the latter, the simulation time value, which represents the time in simulation units before divergence, and a representation of the resulting deformed sphere were used. The maximum simulation time set is 0.1 units, which means that simulations reaching this value have converged. To compare the resulting solution between two simulations, the mean difference of  $J = \det(F)$  is used, which can be calculated as:

$$MD_{12} = \frac{1}{N} \sum_j^N |J_{1j} - J_{2j}|, \quad (27)$$

where  $j$  denotes a particular particle,  $N$  is the total number of particles, and the subindex 1 and 2 refer to two different simulations.

##### 3.1.1. Time step

A sensitivity analysis of the time-step size was performed to establish the stable values needed to correctly discretize time and preserve the physical characteristics of the solution. Four simulations were conducted with the same settings, except for the time step used for the time integration of the different variables. The results can be found in *Table 1*.

Time step	Kernel size (mm)	Simulation's duration	Iteration's duration	Iterations	Simulation time
$0.5 \cdot 10^{-5}$	3.5	47h 33min	8.56s	20000	0.1
$1 \cdot 10^{-5}$	3.5	13h 13min	8.51s	5590	0.0559
$2 \cdot 10^{-5}$	3.5	5h 7min	8.59s	2144	0.0429
$4 \cdot 10^{-5}$	3.5	1h 45min	9.26s	687	0.0275

*Table 1:* Simulation's differences when modifying the time step size. All simulation's geometries presented a number of particles of 32000.

As the time-step size is increased, the simulation's total duration is reduced. In *Figure 6* it can be observed a rapid decrease in running time between using a time-step of size  $0.5 \cdot 10^{-5}$  and  $2 \cdot 10^{-5}$ , which is then stabilized, resembling an exponential decay. Modifying the time-step does not substantially vary the iteration's duration, which can indicate that the decrease in the simulation's duration is due to performing a lower number of iterations.

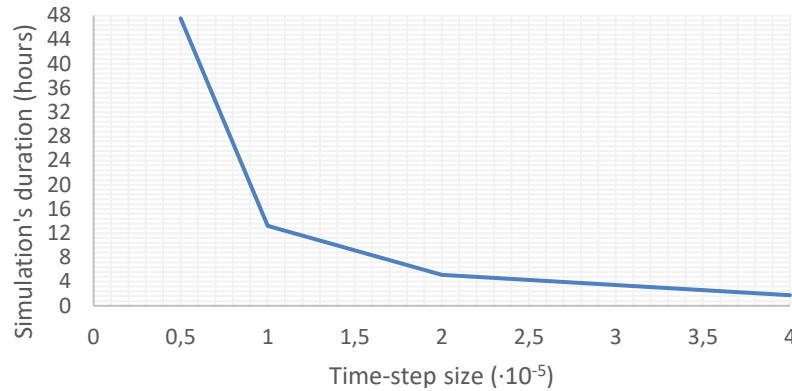


*Figure 6:* Changes in the simulation's total duration when modifying the time-step size.

Regarding the simulations' convergence, the simulation time value differs among settings. Using a time step size of  $0.5 \cdot 10^{-5}$  allows reaching the highest simulation time. Nevertheless, as it is shown in *Figure 7A*, the obtained geometry does not exhibit any deformation. Thus, although the simulation seems to converge, the resulting solution is inaccurate. The opposite behaviour is obtained when using a time-step size of  $4 \cdot 10^{-5}$ : the simulation rapidly diverges, and the resulting deformation is erroneous. The simulations using a time step of  $1 \cdot 10^{-5}$  and  $2 \cdot 10^{-5}$  visually exhibit a similar deformed sphere in their last iteration, with a mean difference of  $J$  of 0.181 units. Nonetheless, neither of the simulations converge because of the presence of particles escaping the geometry. These particles are released from the cortical bulges found in *Figure 7C*, and show the highest  $J$  values. The simulations' divergence is caused by non-invertible deformation gradients in the escaping particles, because the kernel resolution is not large enough to find any neighbours for them. However, the simulation time reached when using a time step of  $1 \cdot 10^{-5}$  units is higher, which can be interpreted as also having a higher convergence. Another feature to point out between these two simulations is the fact that, although the resulting deformation is similar, it is obtained with a lesser simulation time when using a  $2 \cdot 10^{-5}$  time-step. Hence, there is a temporal delay between the two as the test using  $1 \cdot 10^{-5}$  needed a longer simulation time to exhibit the same deformation as the  $2 \cdot 10^{-5}$  test.

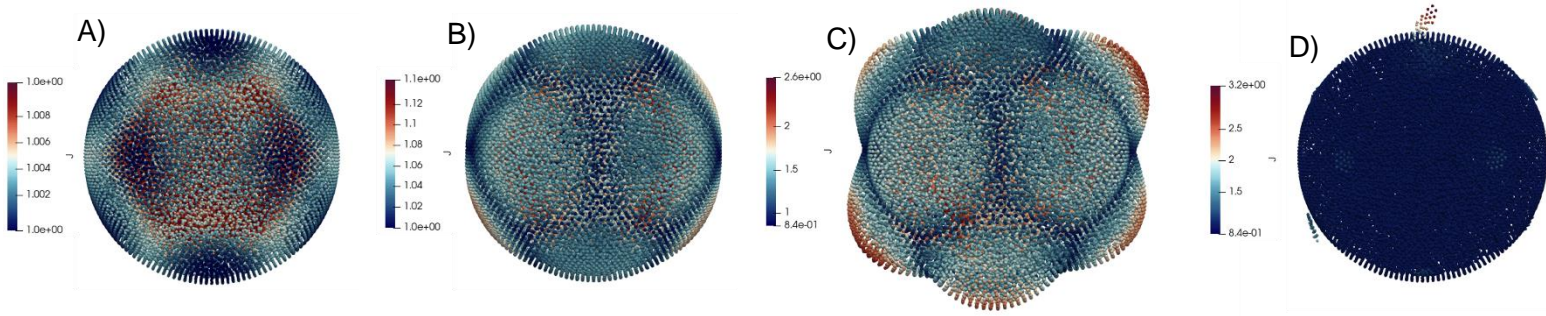


Figure 7: Resulting deformed sphere for each simulation found in simulation time 0.0429 for A, B and C; and simulation time 0.0275 for D. A) Time-step =  $0.5 \cdot 10^{-5}$  B) Time-step =  $1 \cdot 10^{-5}$  C) Time-step =  $2 \cdot 10^{-5}$  D) Time-step =  $4 \cdot 10^{-5}$ . The usage of different axis in each case allows observing that in A there is no deformation, the points of high deformation in B and C (in warmer colours) are found at the same regions, and the escaping particles present the highest J in D.

### 3.1.2. Kernel size

The kernel size study was conducted to set the optimal values to implement the  $C^2$ -Wendland kernel function. In this case, five tests were performed with the same parameter configuration and only changing the kernel size in each simulation. The results can be found in Table 2.

Time step	Kernel size (mm)	Simulation's duration	Iteration's duration	Iterations	Simulation time
$2 \cdot 10^{-5}$	<b>3.0</b>	4h 8min	6.07s	2230	0.0446
$2 \cdot 10^{-5}$	<b>3.5</b>	5h 7min	8.59s	2144	0.0429
$2 \cdot 10^{-5}$	<b>4.0</b>	7h 58min	13.82s	2075	0.0415
$2 \cdot 10^{-5}$	<b>4.5</b>	9h 10min	16.54s	1995	0.0399
$2 \cdot 10^{-5}$	<b>4.75</b>	10h 58min	30.09s	1965	0.0393

Table 2: Simulation's differences when modifying the kernel size. All simulation's geometries presented a number of particles of 32000.

It has been tested kernel size values from 3 mm to 4.75 mm, as a smaller value leads to the usage of an insufficient number of neighbours, especially in the most outer layer, while values higher than 5 mm do not allow even performing the tests because of a lack of computer memory resources. Nevertheless, in the kernel size range tested it was observed that the simulation's duration augments when increasing its value (Figure 8A). In this case, however, the number of iterations performed are similar, which can indicate that the convergence among simulations is comparable and the increase in simulation's duration does not depend on the number of iterations. Moreover, the execution time differences depend on the iteration's duration. As the kernel size augments, more neighbour particles are set for each point, which enlarges the computational cost of the operations performed in each iteration and thus the simulation's execution time. In Figure 8B it can be observed that the iteration's duration grows exponentially for changes in the kernel size parameter.



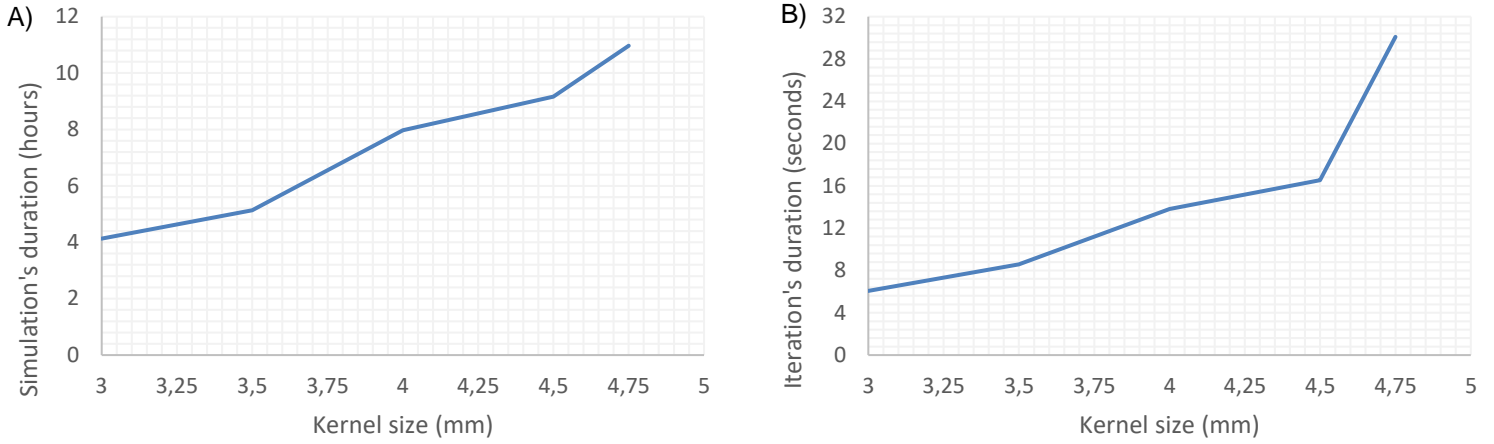


Figure 8: A) Changes of simulation's total duration when modifying the kernel size. B) Changes of iteration's duration for variations of kernel size.

Figure 9 shows a representation of the value of  $J$  for each particle found in a simulation time of 0.0390 in each of the tests. In this case, all spheres are deformed and qualitatively exhibit similar deformation patterns. The highest  $J$  values are found in analogous areas across simulations. In order to quantitatively study the solution's differences among simulations, the test with a kernel size of 4 mm will be used as a reference. Then, the mean difference of  $J$  is computed for all other simulations with respect to the reference. The most similar cases to the reference are found when using a kernel size of 3 mm and 4 mm, with a MD of 0.17 units and 0.22 units respectively. With larger kernel sizes, a higher MD is obtained (0.27 units for a kernel size of 4.5 mm and 0.30 units for a kernel size of 4.75 mm), which it can also be visually corroborated in Figure 9. This can be explained as augmenting the kernel size leads to an increase in the kernel function's range. Therefore, a larger number of particles are taken into account for computing the motion of each point, which has an impact on the obtained solution.

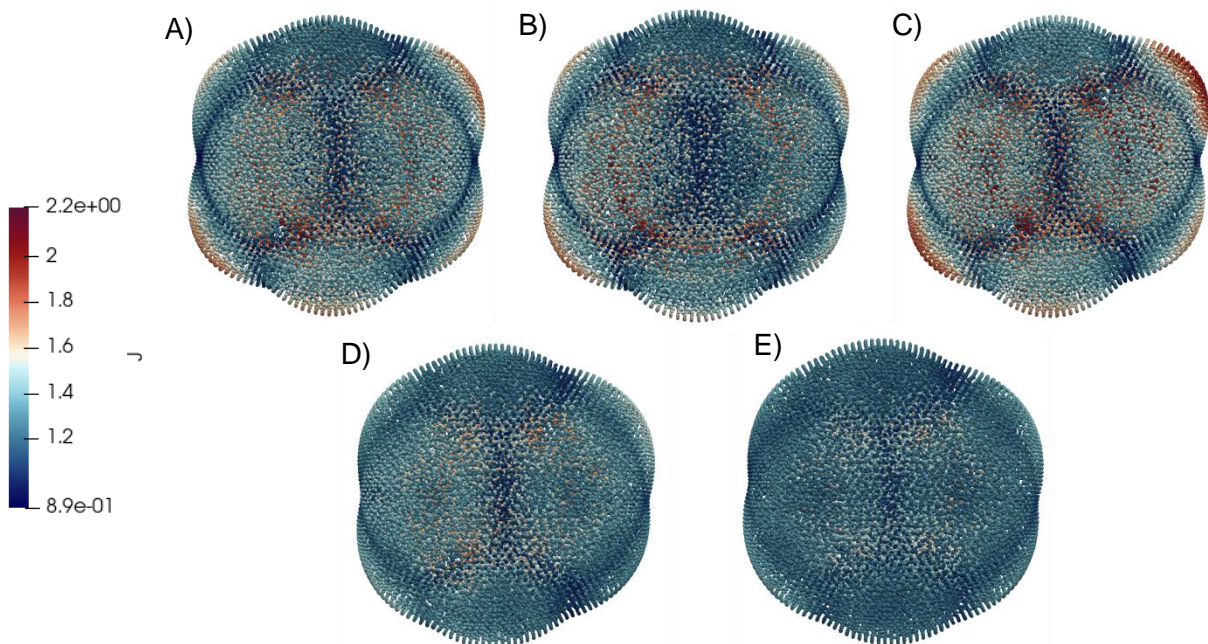


Figure 9: Resulting deformed sphere in each test found in simulation time 0.0390. The higher values of  $J$  (in red) are found on the cortical bulges. A) Kernel size = 3 mm B) Kernel size = 3.5 mm C) Kernel size = 4 mm D) Kernel size = 4.5 mm E) Kernel size = 4.75 mm .

### 3.1.3. Geometry's number of points

For this sensitivity analysis, a time step size of  $2 \cdot 10^{-5}$  and a kernel size of 3.5 were employed. Only three tests were performed since the geometry's generation is a time-consuming step and the intention was to study a situation with a lower number of points (15000) and a higher number of points (45000). The upper limit in number of points found for the computational resources used was of 60000 points. The results can be found in *Table 3*.

Number of particles	Simulation's duration	Iteration's duration	Iterations	Simulation time
15000	1h 18min	3.9s	1200	0.0240
32000	5h 7min	8.59s	2144	0.0429
45000	10h 46min	18.46s	2100	0.0420

*Table 3:* Differences observed when modifying the geometry's number of points.

The variation in particle resolution has an impact on the simulation's total time. As the number of points is increased the total amount of mathematical operations performed also augments, since there are more particles to update, and more neighbours interact with each of the points for the same kernel size. Hence, the computational cost of the simulations is larger, which is reflected in the augmented simulation's duration. To further study this, *Figure 10* presents the relation between the iteration's duration and the number of points. This parameter allows to better compare the tests since in the case of 15000 points the simulation diverged faster, which means that the simulation's duration was also lower because of a smaller number of total iterations performed. The iteration's duration grows faster when increasing the number of points, which is expected to become an exponential growth if tests with more particles could have been performed.

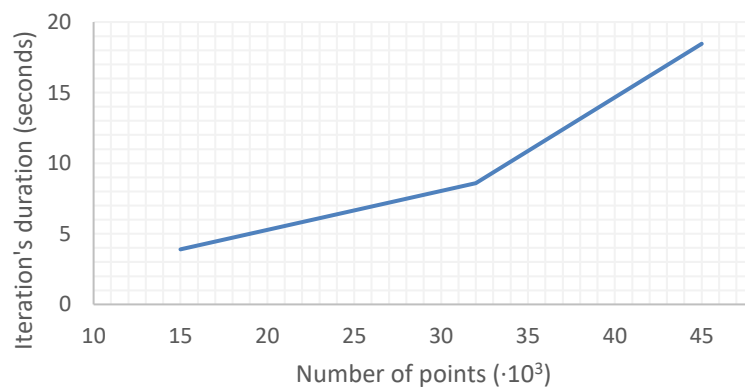


*Figure 10:* Changes of iteration's duration when modifying the geometry's number of particles.

The resulting deformed spheres from each test are shown in *Figure 11*. It is visually appreciated that the deformation patterns differ among simulations, especially in the case of lesser particle resolution (*Fig.11A*). In this test, the simulation diverged faster and the resulting solution is inaccurate. When increasing the number of points, a more recognizable deformation is found.



Furthermore, the potential gain in accuracy when using a higher number of points (*Figure 11C*) leads to a more uniform outer layer deformation with less larger bumps, which was regarded as more desirable. Nevertheless, the kernel definition depends on both the particle resolution and the kernel size. Therefore, the kernel size needs to be adjusted depending on the number of particles used. For instance, the solution presented in *Figure 11A* could be fixed by the usage of a larger kernel size, as more particles would be considered in the kernel function, especially in the external layer.

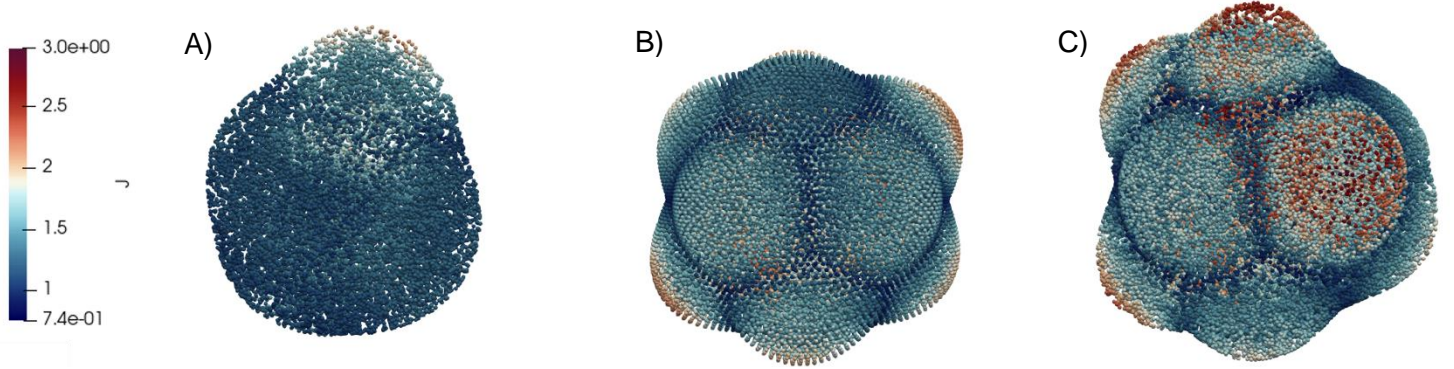


*Figure 11:* Resulting deformed sphere in each test found in simulation time 0.0240 for A; and simulation time 0.0429 for B and C. A) Number of particles = 15000 B) Number of particles = 32000 C) Number of particles = 45000

### 3.1.4. Normal vector direction's interpolation

The initial normal vector of each particle is defined in the pre-simulation step. For each of the tests, the sphere was divided into a different number of portions before applying the interpolation method described in *Section 2.4.2*. The simulations were performed all using the same parameter setting. The results are presented in *Table 4*.

Number of divisions	Simulation's duration	Iteration's duration	Iterations	Simulation time
4	5h	8.41s	2140	0.0428
8	5h 7min	8.59s	2144	0.0429
16	5h 6min	8.54s	2143	0.0429

*Table 4:* Summary of the changes in computational time and convergence observed when changing the interpolation method.

The results show that no major variation in the simulation's duration nor in the solution's convergence are found when changing the number of pieces that the sphere was initially divided before applying the normal vector interpolation algorithm. The computational cost of the tests was expected to be practically equal since all simulations are performed using the same parameter configuration. If the test using 8 divisions is taken as the reference and the mean difference of  $J$  is computed with respect to the other two tests, a  $MD = 0.012$  units for the test using 4 divisions and a  $MD = 0.014$  units for the 16 divisions are obtained, respectively. This

indicates that the resulting deformation pattern in all three tests are nearly equivalent. Therefore, the number of divisions approximation does not have an impact in the obtained solution. This can be qualitatively validated in *Figure 12*. Nevertheless, the pre-processing computational cost needed to do each of the interpolations is different. For a low number of divisions, each particle needs to be compared to a larger number of lines, which increases the computational time needed to obtain a valid meshless geometry. On the other hand, dividing the sphere in a larger number of portions than 8 is also a time-consuming task because it needs to be manually done using Paraview.

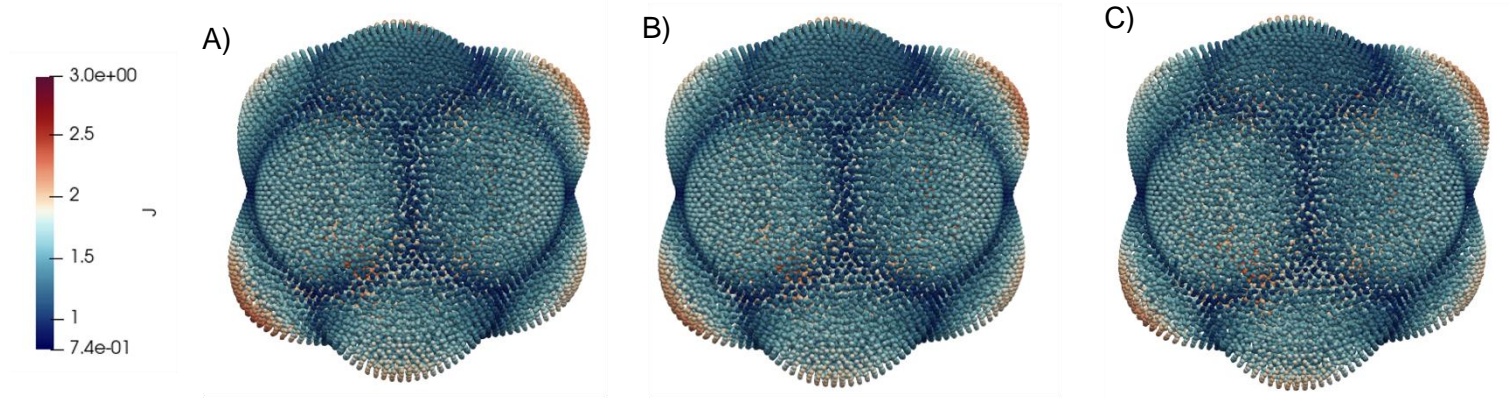


*Figure 12:* Resulting deformed sphere in each test found in simulation time 0.0429.

A) Number of divisions = 4 B) Number of divisions = 8 C) Number of divisions = 16

### 3.2. Comparison between SPH and FEM results

With the intention of comparing the resulting deformed sphere modelled using the SPH formulation, a simulation using FEM methodology was performed. The C++ code employed for running the FEM test was originally presented by Tallinen *et al* in [27], and it was further developed in [28]. In this case, the geometry was initially modelled as a sphere with the same radius as the other tests that have been presented throughout this work and was discretized using a volumetric mesh composed of 223000 elements. For this comparison only two layers were defined, and the shear and bulk modulus remain constant during the course of the simulation. The simulation was performed using a High-Performance Computing (HPC) cluster, which uses 40 CPUs. The FEM test had a total simulation duration of 10.5 minutes. On the other hand, the SPH simulation parameter configuration was set according to the results found on the sensitivity analyses presented in *Section 3.1*. A summary of the simulation's setting is presented in *Table 5*.

Number of points	Time step	Kernel size (mm)	Simulation's duration	Simulation time
45000	$2 \cdot 10^{-5}$	3	7h 23min	0.0430

*Table 5:* SPH simulation and geometry's parameter configuration. In this table it is also displayed the computational time employed and the convergence in terms of the simulation time reached.

The quantitative differences regarding the geometry's growth and surface folding between both tests are examined in terms of cortical layer area, volume and gyrification index. All this metrics were measured in the last iteration of each simulation. The gyrification index allows evaluating the cortical folding by computing the ratio between the deformed area in the final state with respect to the original smooth-surfaced sphere. *Table 6* shows the value of these measures for each simulation. It is observed that the deformed sphere using SPH has 1.6 times more area than the FEM test, while the volume is roughly 0.6 times smaller. This indicates that there is a reduced growth in the SPH model in comparison to the FEM one. The convolution's presence can be measured by evaluating the area to volume ratio. The relation is 2.65 times higher in the SPH, which shows a lower number of surface folds and more cortical bulges. This is further validated by an augmented gyrification index since each of these bulges increases the surface's deformed area.

	Area (mm <sup>2</sup> )	Volume (mm <sup>3</sup> )	Area - Volume ratio (mm <sup>-1</sup> )	Gyrification Index
SPH	11589.99	10895.57	1.06	4.67
FEM	7135.26	17755.59	0.40	1.93

*Table 6:* Quantitative measures for comparing growth and cortical folding between SPH and FEM simulations.

The qualitative evaluation of the deformed spheres allows to further assess the differences between both models. To perform this comparison and better show the obtained results, the solution from the SPH test is transformed into a mesh model (see *Figure 13* and *Figure 14*). This conversion is done in Paraview by using a 3D Delaunay triangulation to build a topological structure from the unconnected, mesh-free particles. This mesh is constructed by fulfilling the Delaunay criterion, which states that a circumsphere of each simplex in a triangulation contains only the defining points of the simplex [42]. By making this meshless-to-mesh transformation, there is an improvement in the visual assessment of the resulting SPH test, as it helps to better compare the obtained deformation pattern to the one found in the FEM test. Nevertheless, is important to point out that the models presented in *Fig.13A*, *Fig.13C*, *Fig.14A* and *Fig.14C* are obtained by meshing the unconnected particles from the SPH solution.

*Figure 13* shows a representation of the interaction between the two simulated layers for both methodologies (*Fig.13A* and *Fig.13C* for SPH, and *Fig.13B* and *Fig.13D* for FEM). In all cases it can be observed that the highest shear modulus is found in the internal layer. Another consistent feature is the separation between cortical and subcortical layers, as there is not any mixture between the two at any point. Nevertheless, there is a tendency of internal particles to grow towards the external part, which shows a cohesion among all the meshless particles. The differences between the two models, which were quantitatively studied previously, are a more

grown geometry in the FEM simulation and the existence of cortical swelling in the SPH test, which is contrasted with a more visually recognizable gyrification pattern that leads to the cortical folding in the FEM simulation.

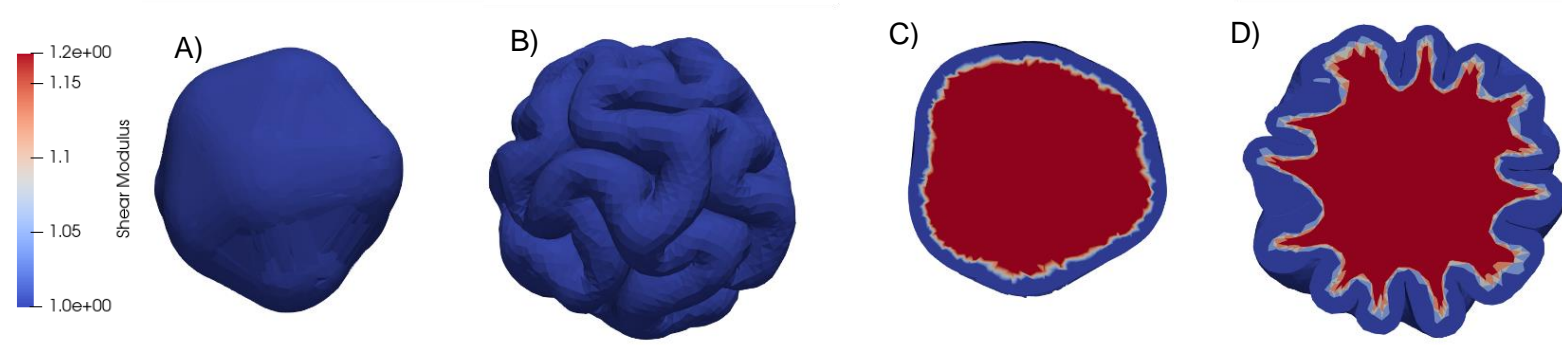


*Figure 13:* Resulting deformed sphere in the last iteration from the SPH model after applying the 3D Delaunay triangulation (A,C), and FEM model (B,D). C and D show the geometry's interior by applying a normal cut with respect to the x axis.

The variations in the deformation pattern between the tests can be studied by analysing the value of  $J$  in the different areas of the geometry. On the one hand, it can be observed that the central area of both simulations remains relatively undeformed, showing a low  $J$ . In the SPH test a spherical nucleus is found in the most central area (*Fig.14C*), while in the FEM simulation this nucleus is less defined, and the most internal part present a similar  $J$  value (*Fig.14D*). The highest subcortical values are found in similar regions of the internal layer: in the SPH case are discerned in the subcortical area under each surface bulge, while in the FEM test are found in the internal part of each gyrus.

Most differences between both simulations are found in the cortex's deformation. The FEM test shows a cortical buckling across the surface produced by its tangential expansion with respect to the internal layer (*Fig.14B*). Moreover, the value of  $J$  is similar in all parts of the cortical region. On the other hand, the SPH simulation presents a different deformation pattern (*Fig.14A*). The appearance of cortical swelling in some surface's regions show a higher value of  $J$  not found in any part of the FEM's cortex, exhibiting in this case a growth in the normal direction. However, the particles that do not form these cortex bulges have a comparable  $J$  with respect to the FEM's cortical layer.

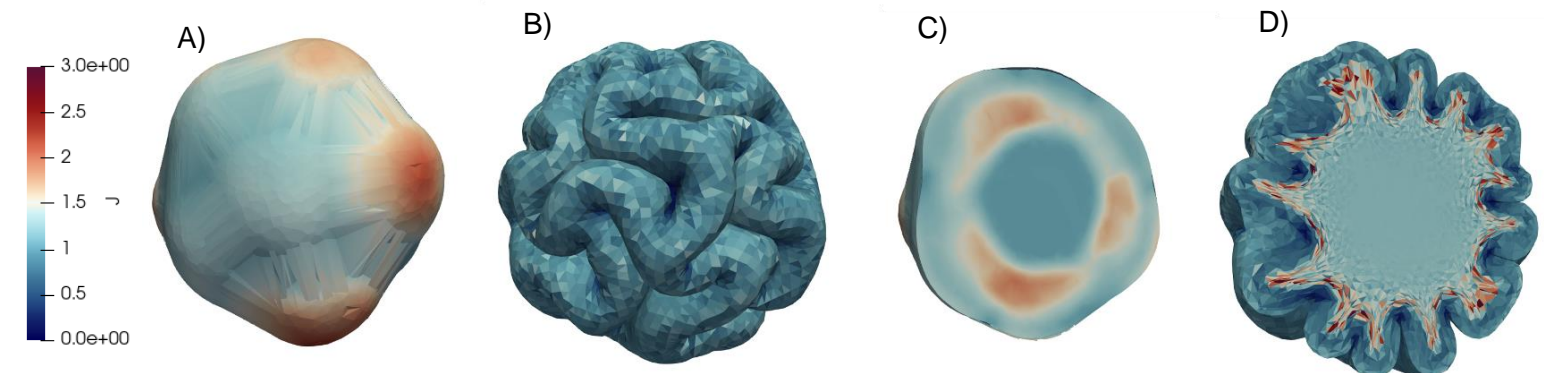


*Figure 14:* Values of  $J$  in the last iteration found in the SPH test after applying the 3D Delaunay triangulation (A,C) and FEM test (B,D). C and D show the geometry's interior by applying a normal cut with respect to the x axis. The highest values of  $J$  are represented in warmer colours.

## 4. DISCUSSION

Due to a recent development in computational power and the enhancement of numerical methods, *in silico* experiments that study the mechanics behind brain's gyrification during early growth have been complemented with computational simulations. The current computational models used in this context are based on the FEM methodology [43], which relies on the definition of highly detailed geometrical meshes in order to discretize the geometry and obtain accurate solutions. This by itself generates a limitation of mesh-based models, as large deformations are produced during cortical folding which lead to overlapping elements that impede obtaining the correct solutions. One possible approach for overcoming these limitations is the usage of meshless computational models, which discretize the domain in independent particles and avoid the problems of mesh degeneration generated by large deformations. Nevertheless, in the literature there is not any mesh-free computational model that integrates the mechanic equations describing brain's gyrification. It is in this context that this project has worked on the first steps for studying brain's cortical folding through a meshless model.

The contributions of this work can be summarized as the development of a pipeline for the pre-processing of mesh geometries to built suitable mesh-free models, the adaptation of a brain's gyrification FEM model so as to be used in a SPH environment, and the development of a parameter setting framework that permits optimizing the solution's accuracy with the total simulation's running time.

### 4.1. Geometries' pre-processing

The construction of patient-specific brain meshless geometries was introduced earlier as one of the project's objectives. Although these geometries were not presented at any point of this work, they were obtained from the work of Alenyà *et al.* [28] and built using the steps described in *Section 2.4.1.* and *Section 2.4.2.* However, they were not used as meshless models due to time limitations, as it was preferred to further develop the mechanical model's integration rather than improving the quality of brain-shaped meshless geometries. Still, the pre-processing pipeline described allowed building functional sphere-shaped meshless models, proving that the process could be adapted to mould any geometry as a meshless model.



## 4.2. Mechanical model inclusion in a SPH environment

The meshless model that has been studied and adapted was proposed by Lluch *et al.* [34], in which the SPH formulation was used to construct a fully coupled multi-physics model of the heart. To start working with this SPH model, all the C++ codes needed to be first integrated and built, which was an obstacle as it required a specific setup for the computational setting I was using. Another difficulty found throughout the project was figuring out the code's organization, as there were not many indications on how to utilize the program. This resulted in employing a large amount of time on just understanding and getting familiar with the SPH environment and all its functionalities, which was a crucial step to comprehend which were the parts of the code that needed to be adapted since it was not obvious while using this extensive code.

Despite these difficulties, the mechanical equations describing brain's cortical folding were integrated inside the program. The physical model used was developed by the adaptation of the gyrification model proposed by Tallinen *et al.* [27] using the SPH formulation and eliminating all boundary conditions that connected the mechanical model to other cardiac solvers. The proposed equations are the consequence of a process of correcting the model by analysing the obtained simulation's solution, which end up being the most time-consuming task. Nevertheless, the original mechanical model could not be integrated in its completeness. The inclusion of the indicator function (*Equation 11*) implied increasing the computational times enormously due to the need of finding the closest cortical point for each of the particles. This limited the modelling to only two tissue types (cortical and subcortical tissue) in contrast to the smooth transition from the cortical layer to the subcortical one found in Tallinen's model.

## 4.3. Sensitivity analyses

The sensitivity analyses were performed with the objective of adjusting several key model and geometry parameters by assessing their impact on the resulting simulation's solution. These analyses defined a parameter framework that permits obtaining accurate solutions in a reasonable time span for the computational resources employed. In the long run, this kind of experiments are key for introducing computational models in a clinical environment, as one of their goals is giving precise, patient-specific information in the least amount of time.

The results showed that the optimal time step size was of  $2 \cdot 10^{-5}$  simulation units. Values smaller than  $1 \cdot 10^{-5}$  units could not appreciate the changes in position and velocity, which resulted in an undeformed sphere (*Fig. 7A*). On the other hand, a time step of  $4 \cdot 10^{-5}$  units was too large and provoked the rapid solution's divergence. It was also observed that the difference in running time between using a time step of  $1 \cdot 10^{-5}$  and  $2 \cdot 10^{-5}$  was of 8 hours 6 min, for

just a mean difference of  $J$  of 0.181 units. Thus, it justified the choice of a time step of  $2 \cdot 10^{-5}$  units.

The kernel size analysis showed an exponential growth of an iteration duration as the parameter was increased (*Fig.8*). This can be explained by an increase in the number of each particles' number of neighbours, which augments the computational cost of the mathematical operations in each iteration, thereby augmenting the simulation's total duration. The resulting solutions presented  $J$  variations, which can also be explained by the increase in the number of particles that have an influence in the kernel function due to augmenting the kernel resolution. Nevertheless, the chosen kernel size was in the range of 3.0 - 3.5 mm because of the balance between a reduced computational time and an appropriate kernel resolution.

The geometry's number of particles also defines the kernel resolution. Hence, the kernel size and the particle resolution need to be adjusted jointly to obtain an optimal kernel resolution. When only changing the geometry's number of points, a nearly exponential growth in running time was observed (*Fig.10*). However, the usage of a higher particle resolution was necessary because of a gain in the deformation's pattern accuracy.

After studying how the number of divisions that the sphere is divided in before applying the interpolation method, it is concluded that the impact on the resulting solution is lower than the other analysed parameters. The parameter's analysis showed a minimal difference in  $J$  among the different tests. Nevertheless, in this case the choice of 8 divisions does not come because of changes in the simulations per se, but due to an augmented computational time during the pre-processing step when using fewer divisions, and the arduous task of manually dividing the sphere for a number of divisions higher than 8, as this step was not completely automatized.

The conclusion of the sensitivity analyses allowed defining the optimal parameters used in the test that compared SPH modelling with a FEM simulation (see *Table 5*). The kernel resolution was adjusted by using a geometry composed of 45000 particles and decreasing the kernel size to 3 mm, which allowed reducing the computational time more than 3 hours with respect to the test using this same number of points and a kernel size of 3.5 mm.

#### **4.4. SPH as a method for modelling brain's gyrification**

The usage of SPH formulation has been shown to be an adequate methodology for modelling large deformations without the need of introducing any penalty function to the model's motion and avoiding mesh distortion. Even though the deformation of a meshless sphere geometry was achieved, the resulting deformed model reveal several differences with respect to the deformed geometry obtained using FEM methods. On the one hand, the total running time required to

complete each simulation largely differed as they were performed using distinct computational resources. The HPC cluster was used to perform the FEM test, which possesses a much higher computational power in comparison to the local resources used for performing all SPH simulations. However, to perform simulations that reproduce accurately the brain's cortical folding using FEM techniques, a mesh of approximately 2 million elements is required, which increase the computational time to more than 30 hours using the HPC cluster resources [28]. Thus, the obtention of accurate solutions using FEM methods can be computationally expensive.

The SPH model is able to replicate the presence of a cortical and subcortical layer, characterized by a different shear modulus ( $\mu$ ), growth rate ( $g$ ) and growth ratio ( $G$ ). Particles that form the inner layer show a similar behaviour as the FEM internal elements, displaying high J values in the transition between cortex and white matter while maintaining a less deformed internal nucleus-like structure.

Regarding the model's cortical behaviour, the gyrification pattern observed along the FEM test's surface is not reproduced in meshless simulations (*Fig.13*). Cortical folds are not formed, but different bulges appear in the external layer instead. This can explain an increased area to volume ratio and an augmented gyrification index (*Table 6*), which in this case is not due to presence of cortical buckling but rather a surface swelling that increases the total deformed area with respect to the original, smooth cortex. Furthermore, these bulges present high J values (*Fig.14A*), which show that the expected tangential expansion of the cortical layer with respect to the subcortical one is not reproduced. Rather, the cortex tends to expand in the normal direction, producing bumps composed of highly deformed particles that tend to escape the geometry and, in the end, cause the solution's divergence. Several hypotheses can be formulated to why the gyrification process is not correctly modelled:

1. The equations used for computing the geometry's deformation are not completely correct. It would be needed to test other approaches for calculating the deformation gradient in order to accurately reproduce the set of equations presented in *Section 2.2*.
2. The implemented values of the mechanical (shear modulus, bulk modulus) and/or growth (growth ratio) parameters are not in the optimal range to obtain the characteristic cortical folding patterns. Performing sensitivity analysis of these parameters would help to see their impact on the resulting deformation patterns.
3. Possible presence of cardiac boundary conditions. These conditions were found dispersed through several parts of the SPH code, and all the encountered ones were substituted. However, it cannot be dismissed the existence of unneeded boundary conditions due to the extensive number of files that built the whole SPH environment.



4. The implemented SPH formulation would need to be refined so as to be used for other applications, as the specific cardiac solvers were more developed than the more general mechanical solver.

## 4.5. Limitations

This work is not without its limitations. As it was commented previously, a sphere model instead of patient-specific brain geometries was employed for all tests performed. This restricted the possibility of validating the resulting solutions with real neonatal MRI data. On the other hand, a model consisting of only two materials (cortex and subcortical tissue) was developed, in contrast to the gradual transition between the two tissue types according to *Equation 11*. Last but not least, the HPC cluster was not used because of time limitations. The usage of a higher computational power could have provided a better spatial resolution for the geometries, more extensive sensitivity analyses and the possibility of diminishing the overall computational time needed for each simulation, which would have been useful to further test the model and enhance the proposed model.

## 5. CONCLUSIONS

This project shows the potential that SPH has for modelling large deformations, which makes it a great candidate for modelling brain's cortical folding during early development. The work also has set the first steps towards building a gyrification meshless model by first developing a pre-processing pipeline to construct functional meshless geometries and then adapting the mechanical equations describing cortical fold formation in an SPH environment. A detailed analysis on the effect of several simulation and geometry parameters for the studied physical was also performed, which helped to set a framework that allowed obtaining precise solutions in a feasible amount of time. However, the obtained cortex deformation pattern in all simulations is not analogous to the one found when using FEM methods. Thus, the integrated biomechanical model needs to be further developed so as to realistically reproduce the gyrification process.



## Bibliography

- [1] Evertz, K., Janus, L., Linder, R., & Beate Skoruppa, D. (2009). Handbook of prenatal and perinatal psychology (pp. 4-16)
- [2] Tatishvili, N., Gabunia, M., Laliani, N., & Tatishvili, S. (2010). Epidemiology of neurodevelopmental disorders in 2 years old Georgian children. Pilot study – population based prospective study in a randomly chosen sample. *European Journal Of Paediatric Neurology*, 14(3), 247-252. <https://doi.org/10.1016/j.ejpn.2009.07.004>
- [3] Lawn, J., Kerber, K., Enweronu-Laryea, C., & Cousens, S. (2010). 3.6 Million Neonatal Deaths—What Is Progressing and What Is Not?. *Seminars In Perinatology*, 34(6), 371-386. <https://doi.org/10.1053/j.semperi.2010.09.011>
- [4] Synnes, A., Anson, S., Arkesteijn, A., Butt, A., Grunau, R., Rogers, M., & Whitfield, M. (2010). School Entry Age Outcomes for Infants with Birth Weight  $\leq 800$  Grams. *The Journal Of Pediatrics*, 157(6), 989-994.e1. <https://doi.org/10.1016/j.jpeds.2010.06.016>
- [5] Garcia, K., Robinson, E., Alexopoulos, D., Dierker, D., Glasser, M., & Coalson, T. et al. (2018). Dynamic patterns of cortical expansion during folding of the preterm human brain. *Proceedings Of The National Academy Of Sciences*, 115(12), 3156-3161. <https://doi.org/10.1073/pnas.1715451115>
- [6] Garcia, K., Kroenke, C., & Bayly, P. (2018). Mechanics of cortical folding: stress, growth and stability. *Philosophical Transactions Of The Royal Society B: Biological Sciences*, 373(1759), 20170321. <https://doi.org/10.1098/rstb.2017.0321>
- [7] Ono, M., Kubik, S., & Abernathey, C. (1990). *Atlas of the cerebral sulci*. G. Thieme Verlag.
- [8] Kroenke, C., & Bayly, P. (2018). How Forces Fold the Cerebral Cortex. *The Journal Of Neuroscience*, 38(4), 767-775. <https://doi.org/10.1523/jneurosci.1105-17.2017>
- [9] Jones, E., & Peters, A. (1990). *Comparative structure and evolution of cerebral cortex*. Plenum Press.
- [10] Barron, D. (1950). An experimental analysis of some factors involved in the development of the fissure pattern of the cerebral cortex. *Journal Of Experimental Zoology*, 113(3), 553-581. <https://doi.org/10.1002/jez.1401130304>
- [11] Xu, G., Knutsen, A., Dikranian, K., Kroenke, C., Bayly, P., & Taber, L. (2010). Axons Pull on the Brain, But Tension Does Not Drive Cortical Folding. *Journal Of Biomechanical Engineering*, 132(7). <https://doi.org/10.1115/1.4001683>
- [12] Essen, D. (1997). A tension-based theory of morphogenesis and compact wiring in the central nervous system. *Nature*, 385(6614), 313-318. <https://doi.org/10.1038/385313a0>
- [13] Dehay, C., Giroud, P., Berland, M., Killackey, H., & Kennedy, H. (1996). Phenotypic characterisation of respecified visual cortex subsequent to prenatal enucleation in the monkey: Development of acetylcholinesterase and cytochrome oxidase patterns. *The Journal Of Comparative Neurology*, 376(3), 386-402. [https://doi.org/10.1002/\(sici\)1096-9861\(19961216\)376:3<386::aid-cne3>3.0.co;2-z](https://doi.org/10.1002/(sici)1096-9861(19961216)376:3<386::aid-cne3>3.0.co;2-z)

- [14] Xu, G., Bayly, P., & Taber, L. (2008). Residual stress in the adult mouse brain. *Biomechanics And Modeling In Mechanobiology*, 8(4), 253-262. <https://doi.org/10.1007/s10237-008-0131-4>
- [15] Toro, R., & Burnod, Y. (2005). A Morphogenetic Model for the Development of Cortical Convolutions. *Cerebral Cortex*, 15(12), 1900-1913. <https://doi.org/10.1093/cercor/bhi068>
- [16] Stiles, J., & Jernigan, T. (2010). The Basics of Brain Development. *Neuropsychology Review*, 20(4), 327-348. <https://doi.org/10.1007/s11065-010-9148-4>
- [17] Lui, J., Hansen, D., & Kriegstein, A. (2011). Development and Evolution of the Human Neocortex. *Cell*, 146(2), 332. <https://doi.org/10.1016/j.cell.2011.07.005>
- [18] Fernández, V., Llinares-Benadero, C., & Borrell, V. (2016). Cerebral cortex expansion and folding: what have we learned?. *The EMBO Journal*, 35(10), 1021-1044. <https://doi.org/10.15252/embj.201593701>
- [19] Borrell, V., & Reillo, I. (2012). Emerging roles of neural stem cells in cerebral cortex development and evolution. *Developmental Neurobiology*, 72(7), 955-971. <https://doi.org/10.1002/dneu.22013>
- [20] Juan Romero, C., Bruder, C., Tomasello, U., Sanz-Anquela, J., & Borrell, V. (2015). Discrete domains of gene expression in germinal layers distinguish the development of gyrencephaly. *The EMBO Journal*, 34(14), 1859-1874. <https://doi.org/10.15252/embj.201591176>
- [21] Greiner, A., Kaessmair, S., & Budday, S. (2021). Physical aspects of cortical folding. *Soft Matter*, 17(5), 1210-1222. <https://doi.org/10.1039/d0sm02209h>
- [22] Striedter, G., Srinivasan, S., & Monuki, E. (2015). Cortical Folding: When, Where, How, and Why?. *Annual Review Of Neuroscience*, 38(1), 291-307. <https://doi.org/10.1146/annurev-neuro-071714-034128>
- [23] Tallinen, T., Chung, J., Biggins, J., & Mahadevan, L. (2014). Gyrification from constrained cortical expansion. *Proceedings Of The National Academy Of Sciences*, 111(35), 12667-12672. <https://doi.org/10.1073/pnas.1406015111>
- [24] Toro, R. (2012). On the Possible Shapes of the Brain. *Evolutionary Biology*, 39(4), 600-612. <https://doi.org/10.1007/s11692-012-9201-8>
- [25] Bayly, P., Taber, L., & Kroenke, C. (2014). Mechanical forces in cerebral cortical folding: A review of measurements and models. *Journal Of The Mechanical Behavior Of Biomedical Materials*, 29, 568-581. <https://doi.org/10.1016/j.jmbbm.2013.02.018>
- [26] Weickenmeier, J., de Rooij, R., Budday, S., Ovaert, T., & Kuhl, E. (2017). The mechanical importance of myelination in the central nervous system. *Journal Of The Mechanical Behavior Of Biomedical Materials*, 76, 119-124. <https://doi.org/10.1016/j.jmbbm.2017.04.017>
- [27] Tallinen, T., Chung, J., Rousseau, F., Girard, N., Lefèvre, J., & Mahadevan, L. (2016). On the growth and form of cortical convolutions. *Nature Physics*, 12(6), 588-593. <https://doi.org/10.1038/nphys3632>

- [28] Alenyà, M., Wang, X., Lefèvre, J., Auzias, G., Fouquet, B., Eixarch, E., Rousseau, F., Camar, O. (2021). Computational pipeline for the generation and validation of patient-specific mechanical models of brain development.
- [29] Dervaux, J., & Ben Amar, M. (2008). Morphogenesis of Growing Soft Tissues. *Physical Review Letters*, 101(6). <https://doi.org/10.1103/physrevlett.101.068101>
- [30] Hong, W., Zhao, X., & Suo, Z. (2009). Formation of creases on the surfaces of elastomers and gels. *Applied Physics Letters*, 95(11), 111901. <https://doi.org/10.1063/1.3211917>
- [31] Reddy, J. Introduction to the finite element method.
- [32] Wang, X., Lefèvre, J., Bohi, A., Harrach, M., Dinomais, M., & Rousseau, F. (2021). The influence of biophysical parameters in a biomechanical model of cortical folding patterns. *Scientific Reports*, 11(1). <https://doi.org/10.1038/s41598-021-87124-y>
- [33] Wang, X., Bohi, A., Harrach, M.A., Dinomais, M., Lefevre, J., Rousseau, F., (2019). On early brain folding patterns using biomechanical growth modeling.
- [34] Lluch, È., De Craene, M., Bijmens, B., Sermesant, M., Noailly, J., Camara, O., & Morales, H. (2019). Breaking the state of the heart: meshless model for cardiac mechanics. *Biomechanics And Modeling In Mechanobiology*, 18(6), 1549-1561. <https://doi.org/10.1007/s10237-019-01175-9>
- [35] J, B. (2016). Meshless Methods: The Future of Computational Biomechanical Simulation. *Journal Of Biometrics & Biostatistics*, 07(04). doi: 10.4172/2155-6180.1000325
- [36] Doweidar, M., Calvo, B., Alfaro, I., Groenenboom, P., & Doblaré, M. (2010). A comparison of implicit and explicit natural element methods in large strains problems: Application to soft biological tissues modeling. *Computer Methods In Applied Mechanics And Engineering*, 199(25-28), 1691-1700. doi: 10.1016/j.cma.2010.01.022
- [37] Doblaré, M., Cueto, E., Calvo, B., Martínez, M., Garcia, J., & Cegoñino, J. (2005). On the employ of meshless methods in biomechanics. *Computer Methods In Applied Mechanics And Engineering*, 194(6-8), 801-821. doi: 10.1016/j.cma.2004.06.031
- [38] Tsubota, K., Wada, S., & Yamaguchi, T. (2006). Particle method for computer simulation of red blood cell motion in blood flow. *Computer Methods And Programs In Biomedicine*, 83(2), 139-146. doi: 10.1016/j.cmpb.2006.06.005
- [39] Ericson, C. (2005). Real-Time Collision Detection.
- [40] Rabczuk, T., Belytschko, T., and Xiao, S. P. (2004). Stable particle methods based on Lagrangian kernels. *Comput. Methods Appl. Mech. Eng.*, 193(12- 14):1035–1063.
- [41] He, L. and Seaid, M. (2016). A Runge–Kutta–Chebyshev SPH algorithm for elastodynamics. *Acta Mech.*, 227(7):1813–1835.
- [42] Klyachin, V., & Shirokii, A. (2011). The Delaunay triangulation for multidimensional surfaces and its approximative properties. *Russian Mathematics*, 56(1), 27-34. doi: 10.3103/s1066369x12010045

- [43] Hickmott, R., Bosakhar, A., Quezada, S., Barresi, M., Walker, D., & Ryan, A. et al. (2021). The One-Stop Gyrification Station - Challenges and New Technologies. *Progress In Neurobiology*, 204, 102111. doi: 10.1016/j.pneurobio.2021.102111